Air-Bleed Aerodynamics: A Mesh-Sensitivity CFD Study of Pressure, Turbulence, and Heat in a Synthetic Shuttlecock

Abdullah Riaz[1], Sana Ullah[1]*, Saqib Khan[1], Sayed Rahiq Ahmad[1], Suffiullah Qaisar[1], Asad Ullah[2], Intikhab Khan[1]

[1]Department of Mechanical Engineering, University of Engineering and Technology, Peshawar 25120, Pakistan

[2]Department of Mechanical Engineering, University of Engineering and Technology, Mardan 23200, Pakistan

*Correspondence: sanaullah.uet31@gmail.com

Citation | Riaz. A, Ullah. S, Khan. S, Ahmad. S. R, Qaisar. S, Ullah. A, Khan. I, "Air-Bleed Aerodynamics: A Mesh-Sensitivity CFD Study of Pressure, Turbulence, and Heat in a Synthetic Shuttlecock", IJIST, Vol. 8 Issue. 9 pp 3859-3876, October 2026

Received | Oct 07, 2026 **Revised |** Oct 25, 2026 **Accepted |** Oct 27, 2026 **Published |** Oct 29, 2026.

This study presents a steady-state computational fluid dynamics (CFD) investigation of the airflow around a porous synthetic badminton shuttlecock. The study aims to quantify drag, surface pressure, wall shear stress, turbulence, and temperature, and to assess how sensitive these quantities are to mesh resolution. An explicit three-dimensional multi-body CAD model, including the micro-pore windows of the skirt, was simulated in SolidWorks Flow Simulation at a freestream velocity of 20 m/s (Reynolds number Re = 8.7×10^4, air at 101,325 Pa) with a modified k–ε turbulence model. Three Cartesian cut-cell meshes of 4,177, 11,840 and 127,646 cells gave averaged drag forces of 1.259 N, 7.299 N and 6.269 N, respectively. The drag response is oscillatory rather than monotonic, and the 14.1 % difference between the medium and fine meshes shows that mesh independence has not yet been achieved, so the work is reported as a mesh-sensitivity study. On the fine mesh, the peak surface pressure was 101,421.94 Pa (96.94 Pa above ambient, a pressure coefficient of 0.40), the peak wall shear stress was 2.41 Pa, the maximum local velocity was 21.904 m/s, and the peak static temperature was 293.39 K, which is consistent with the stagnation temperature rise of about 0.2 K expected from the energy equation. For a shuttlecock with a 66 mm skirt diameter, the predicted drag corresponds to a drag coefficient far above the published values of about 0.5-0.7, so the absolute force is not validated and only the qualitative flow features are considered reliable. These features are a stagnation zone on the nose cap, a low-pressure recirculation wake, and air bleed through the skirt pores. The study provides a documented baseline and a clear refinement and validation path for the CFD-based design of synthetic shuttlecocks.

Keywords: Aerodynamics, Computational Fluid Dynamics, Mesh Sensitivity, Synthetic Shuttlecock, Porous Bluff Body, Subsonic Flow.

Introduction:

The aerodynamic behavior of a badminton shuttlecock is unusual among sports projectiles. Its drag is high enough to decelerate it rapidly, yet it settles quickly into stable, nose-first flight [1][2][3]. This behavior comes from its two-part construction: a dense cork nose that places the center of mass forward, and a light, porous conical skirt that produces drag and places the center of pressure behind the center of mass [1][4]. Feather shuttlecocks are permeable because air passes through the gaps between the feather shafts, and synthetic shuttlecocks reproduce this permeability with a molded skirt that contains windows or slots [4][5][6]. Synthetic shuttlecocks are cheaper and more durable, but manufacturers have long struggled to match the flight of feather shuttlecocks [1]. Because the flow through the skirt gaps (the air bleed) changes the pressure difference across the skirt, it has a first-order effect on drag.

Experimental and numerical studies have established the main effects. Wind-tunnel drag coefficients of feather shuttlecocks vary widely, from about 0.48 to 0.74, and part of the scatter has been linked to the sting mounts used in testing [1], [2], [4]. [5] used CFD to show that skirt gaps raised drag by up to 45.2% relative to a gapless cone, with a 3.2–4.7% difference between simulated and measured drag for the gapless case, and Hasegawa et al. [3] likewise related the high drag of a standard shuttlecock to the flow through its gaps. [4] reported the first CFD simulations of a geometrically realistic feather shuttlecock and compared turbulence modeling approaches, and [7] extended this with scale-resolving simulations, finding that rotation lowers drag and that drag was independent of Reynolds number.

Studies from 2022 to 2026 have broadened the scope. [8] coupled the airflow and the skirt deformation of a nylon shuttlecock in a two-way fluid-structure simulation and found that the skirt deforms inwards as speed increases, which reduces the flow through the shuttlecock and gives much lower drag than a rigid skirt. [9] used CFD to compare feather, nylon and synthetic shuttlecocks at several pitch angles and reported a drag coefficient of about 0.56 for the feather and foam designs. [10] measured drag, lift and pitching force in a wind tunnel at 10–50 m/s and reported that sealing the skirt gaps reduced drag by up to 10 %, and that simulated trajectories matched measurements within 5 %. [11] examined how gaps influence turnover stability, [12] related CFD drag to trajectory parameters, [13] studied trajectories during spin serves, and [14] and [15] compared feather and synthetic shuttlecocks experimentally. The development of shuttlecock design has been reviewed in [16].

Taken together, these works show that (i) drag is strongly controlled by the air bleed through the skirt, (ii) published drag coefficients depend on the test or modeling method, and (iii) most recent work concentrates on forces, trajectories and skirt flexibility. To the authors' knowledge, two points are not usually reported together in one study: the spatial distribution of surface pressure, wall shear stress, turbulence and temperature on an explicitly modeled porous skirt, and the sensitivity of the predicted forces to mesh resolution for such a thin-walled, perforated geometry. Studies that replace the skirt by a homogeneous porous zone avoid meshing the pores, but they cannot resolve the local flow through individual windows [17].

The research gap addressed here is therefore a combined, quantitative description of the pressure, shear, turbulence and thermal fields on an explicitly modeled porous synthetic shuttlecock, together with an explicit assessment of how far the predicted drag depends on mesh resolution. This matters for two reasons. First, design guidance that links skirt porosity to local flow is needed if synthetic shuttlecocks are to be made to fly like feather ones [1]. Second, a CFD model that is mesh-sensitive cannot be used to compare designs until its numerical error is quantified.

To address this gap, this study simulates steady external flow around an explicit three-dimensional parametric synthetic shuttlecock assembly in SolidWorks Flow Simulation at 20

m/s along the primary axis. The drag force F_d and the perpendicular lift force F_l are monitored, and a lift force that is small relative to drag is used as a check of flow symmetry. Velocity, pressure, temperature and turbulence cut plots and flow trajectories are used to examine the wake, and three meshes of 4,177 to 127,646 cells are used to test mesh sensitivity.

Novelty of the Present Study:

The novelty of this work lies in the combination of four elements that are not usually reported together: (i) an explicit, parametric multi-body CAD model of a synthetic shuttlecock in which the rectangular and trapezoidal skirt windows are geometrically resolved, rather than replaced by a porous-media zone; (ii) a three-level mesh study with drag, lift and surface fields reported for each level, including the case in which the response is oscillatory; (iii) a multiphysical output set covering surface pressure, wall shear stress, velocity, turbulence and temperature from a single simulation; and (iv) a transparent comparison with published drag coefficients that states where the present model does and does not agree. The aim is not a new flow solver but a documented, reproducible baseline for the design of porous skirts.

Research Objectives:

In line with the title, the objectives of this study are:

Drag and lift: to determine the aerodynamic drag and lift forces on an explicitly modeled porous synthetic shuttlecock at 20 m/s.

Pressure: to map the surface pressure and identify the stagnation, expansion and air-bleed regions.

Turbulence and thermal behavior: to characterize the velocity, turbulence and temperature fields in the wake, and to compare the peak temperature with the energy-equation estimate.

Mesh independence: to assess the sensitivity of the drag to mesh resolution on three meshes and to quantify the difference between successive meshes.

Model accuracy: to compare the predicted drag with published shuttlecock data and to state the limits of the current model.

Literature Review and Theoretical Background:

Aerodynamics of Porous Sports Projectiles:

A shuttlecock is a porous conical bluff body: a solid hemispherical dome precedes a thin-walled conical skirt that is perforated by gaps [4]. The wind-tunnel measurements of Cooke [1] covered Reynolds numbers (based on the maximum skirt diameter) from about 13,000 to 190,000, corresponding to 3-44 m/s, and gave drag, lift and pitching-moment coefficients for feather and synthetic shuttlecocks. [2] found that feather shuttlecocks had lower drag coefficients at low speed and higher drag coefficients at high speed, whereas synthetic shuttlecocks showed the opposite trend, which they attributed to skirt deformation. Reported drag coefficients for feather shuttlecocks range from 0.48 to 0.74, and [4] note that a sting mount behind the shuttlecock base disturbs the internal flow and may explain part of this scatter. For comparison, a solid cone with a 20° half angle has a drag coefficient of about 0.43 [4], so porosity raises drag relative to a solid cone. Air passing through the gaps meets the external flow at the end of the skirt; [5] showed that gaps raise the pressure difference between the inner and outer skirt surfaces and so increase drag, up to a critical gap size, beyond which drag decreases, and [10] measured a drag reduction of up to 10 % when gaps were sealed.

Boundary-Layer Development and Flow Separation:

For Reynolds numbers of the order of 10^4-10^5, which include the 20 m/s case studied here (Eq. (4)), the boundary layer on the nose cap is thin. The wall shear stress τ_w [Pa] follows from the dynamic viscosity μ [Pa·s] and the wall-normal gradient of the streamwise velocity v_x [m/s] at the wall, where y [m] is the distance normal to the wall:

$$\tau_w = \mu \, (\partial v_x / \partial y)_{y=0} \qquad (1)$$

On a smooth bluff body, an adverse pressure gradient ($\partial p / \partial x > 0$) slows the near-wall fluid until the wall gradient vanishes, which marks the separation point:

$$(\partial v_x/\partial y)_{y=0} = 0 \quad (2)$$

Separation produces a wide low-pressure wake and therefore pressure (form) drag. In a perforated skirt, air bleeding through the windows can inject momentum into the near-wall and wake regions and change the separation location and wake structure; the experiments and simulations in [3][5] attribute the higher drag of a gapped shuttlecock to this through-flow and to the resulting pressure difference across the skirt.

Porous Media Approximations:

Because the skirt contains many thin, closely spaced gaps, an alternative to meshing every gap is to replace the skirt by a homogeneous porous zone, in which the momentum loss per unit volume is added to the Navier–Stokes equations through the Darcy–Forchheimer source term S_i [N/m^3] [17]:

$$S_i = -(\mu/a \cdot v_i + C_2 \cdot \tfrac{1}{2} \varrho \, |v| \, v_i) \quad (3)$$

where v_i is the velocity component [m/s] in direction i, $|v|$ is the velocity magnitude [m/s], ϱ is the air density [kg/m^3], μ is the dynamic viscosity [Pa·s], α is the permeability of the medium [m^2] and C_2 is the inertial resistance factor [1/m]. This approach is efficient and has been applied to open-cell porous metals [17], but the porous zone contains no individual windows, so it cannot show the local jets, shear layers and pressure peaks that form at each window. Explicitly meshed models, as used in [4][5], therefore remain necessary when the aim is to examine the local air-bleed flow, which motivates the explicit geometry adopted here.

Turbulence and Wake Characteristics:

Reynolds-averaged Navier–Stokes (RANS) models are the most economical way to simulate this flow. [4] compared turbulence modeling approaches for a feather shuttlecock with steady RANS, and [7] used scale-resolving simulation to capture unsteady structures that steady RANS cannot. [4] also note that steady RANS studies give a starting point for understanding the flow but do not fully reveal its complex structure.

Two consequences are relevant to the present work. First, a steady RANS solution represents the mean flow only, so wake unsteadiness and vortex shedding are not resolved. Second, turbulence quantities such as turbulence intensity and turbulence length are model outputs, and they indicate where turbulence is produced rather than giving measured values.

Thermal Behavior at Low Speed:

At 20 m/s the temperature changes in air are small. Conversion of kinetic energy to enthalpy at a stagnation point raises the temperature by $\Delta T_0 = U^2/(2c_p)$, which is about 0.20 K for U = 20 m/s and c_p = 1005 J/(kg·K). Temperature fields in this flow therefore reflect pressure–velocity (energy-equation) coupling rather than significant frictional heating, and they are used here as a consistency check on the solved energy balance.

Grid Convergence and CFD Verification:

Discretization error should be quantified before a CFD result is interpreted. [18] introduced the Grid Convergence Index (GCI) based on Richardson extrapolation, and [19] recommended a procedure that uses three systematically refined grids with a refinement ratio above 1.3: the apparent order of convergence and the extrapolated value are computed from the three solutions, and the type of convergence is identified from the ratio $R = (\varphi_{fine} - \varphi_{medium})/(\varphi_{medium} - \varphi_{coarse})$ of successive solution differences. Monotonic convergence ($0 < R < 1$) allows the GCI to be calculated, whereas oscillatory convergence ($R < 0$) or divergence ($R > 1$) means that the grids are not in the asymptotic range and the GCI cannot be applied reliably [19]. Mesh resolution can change the predicted forces on bluff bodies, as reviewed in [20] and shown for a finite rectangular prism in [21], and Cartesian cut-cell meshing has been used to preserve the geometry of complex boundaries [22].

Table 1 compares the main experimental and numerical studies of shuttlecock aerodynamics and identifies the research gaps addressed by the present work.

Table 1. Critical Comparison of Previous Experimental and Numerical Shuttlecock Studies

Ref	Method	Focus	Key finding	Open point relevant to present work
[1]	Wind tunnel, 13,000 < Re < 190,000	Drag, lift and pitching-moment coefficients	Complete coefficient data for feather and synthetic shuttlecocks	Forces only; no local pressure, shear or temperature fields
[2]	Wind tunnel, 60–120 km/h	Drag coefficient versus speed	Feather: lower drag at low speed, higher at high speed; synthetic: opposite	Skirt deformation suspected but flow field not resolved
[4]	Steady RANS, realistic feather shuttle	Turbulence-model comparison; drag coefficient	First CFD of a realistic feather shuttle; wind-tunnel C_d range 0.48–0.74 noted	Feather shuttle; thermal fields and mesh sensitivity not the focus
[5]	CFD with wind-tunnel check	Gap size versus drag	Gaps raise drag by up to 45.2 %; 3.2-4.7 % CFD-experiment difference (gapless cone)	Gap-size study; no turbulence or temperature mapping
[7]	Scale-resolving simulation with rotation	Drag coefficient and flow structures	Rotation lowers C_d; C_d independent of Re	Feather shuttle at high cost; no thermal mapping
[8]	Two-way fluid-structure interaction	Skirt deformation and drag	Skirt deforms inwards with speed; much lower drag than a rigid skirt	Flexible nylon skirt; rigid-skirt mesh sensitivity not addressed
[9]	CFD at several pitch angles	Drag and lift coefficients	$C_d \approx 0.56$ for feather and foam shuttlecocks	Force coefficients only
[10]	Wind tunnel, 10–50 m/s, with trajectory model	Forces, gaps, trajectories	Sealing gaps cuts drag by up to 10 %; trajectories within 5 %	Experimental; local fields not mapped

Methodology:

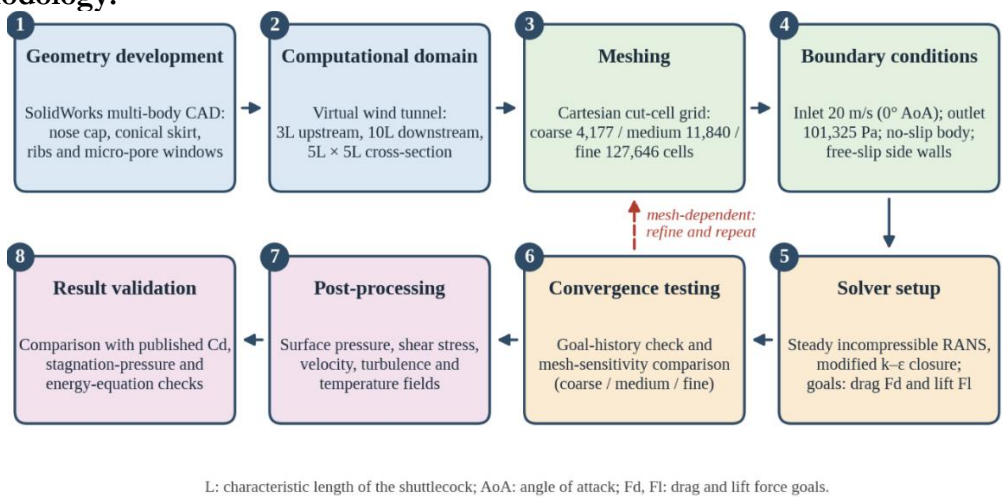

Figure 1. Methodology flowchart of the CFD study: (1) geometry development, (2) computational domain, (3) meshing, (4) boundary conditions, (5) solver setup, (6) convergence and mesh-sensitivity testing with a refinement loop, (7) post-processing, and (8) result validation.

The computational pipeline used to evaluate the fluid dynamics of the multi-body synthetic structure is illustrated in Figure 1. It has eight steps: geometry development,

definition of the computational domain, meshing, boundary conditions, solver setup, convergence and mesh-sensitivity testing, post-processing, and result validation against published data.

Geometric Configuration and Multi-Body CAD Generation:

The model was developed as a parametric multi-body assembly in SolidWorks (Figure 2). A two-dimensional profile of a solid hemispherical nose cap was revolved about the longitudinal axis. The conical skirt was generated by lofting between offset planes perpendicular to the flight axis, which defined the increase in diameter along the skirt, and thin-walled stems and a ring frame were added. Rectangular and trapezoidal windows were cut through the skirt walls with cut-extrude features to represent the porosity of a synthetic skirt, and a circular pattern about the axis completed the assembly as a rigid, watertight multi-body part ready for meshing. The skirt was treated as rigid, so skirt deformation, which is important for nylon shuttlecocks at higher speed [8], is not modeled. The principal dimensions are given in Table 2.

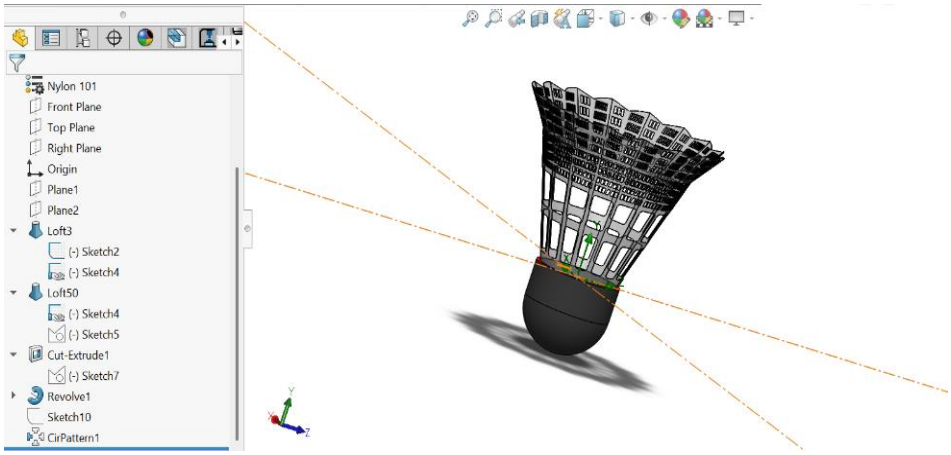

Figure 2. High-fidelity multi body CAD model assembly of the synthetic shuttlecock showing the hemispherical nose cap and porous micro lattice skirt geometry.

To define the fluid-flow region around the structure, the model was enclosed within a virtual wind tunnel known as the computational domain. The domain size was set as multiples of \(L\), the characteristic length of the shuttlecock, defined as its total height, as listed in Table 2. The inlet is located 3L upstream to ensure that the incoming uniform flow is not affected by the stagnation region, the outlet is 10L downstream to contain the recirculation wake, and the lateral walls are 5L apart so that blockage is small. The ratio of the frontal area ($\pi D^2/4$) to the cross-section area $(5L)^2$ is $0.031(D/L)^2$, which is about 2 % for $D/L \approx 0.77$, the proportions of the shuttlecock in [4]. The downstream distance is of the same order as the 12H used for a shuttlecock domain in [7].

Table 2. Geometric Dimensions and Computational Domain Specifications

Parameter	Value / Scaling	Purpose or basis
Total height (characteristic length, L)	86 mm	Reference length for the domain scaling
Nose cap diameter	66 mm	Hemispherical cork head
Maximum skirt diameter (D)	27 mm	Reference length for Re; reference area for C_d
Skirt length	62 mm	Conical skirt between nose cap and ring frame
Number of stems (ribs)	16	Structural frame of the skirt
Rectangular window size (width × height)	7 mm × 20 mm	Air-bleed pore

Trapezoidal window size (bases × height)	2 mm × 3 mm × 5 mm	Air-bleed pore
Wall and stem thickness	1 mm	Thin-walled skirt structure
Skirt open-area ratio (window area / skirt area)	35 %	Porosity of the skirt
Upstream inlet distance	3×L	Allows the incoming flow to stabilize before impact
Downstream outlet distance	10×L =	Provides adequate space to fully resolve the turbulent wake
Domain cross-section	5×L by 5×L	Eliminates lateral wall blockage effects
Blockage ratio	0.031 $(D/L)^2$ ≈=2 % for D/L = 0.77	Frontal area divided by cross-section area

Fluid Domain Discretization (Meshing):

The fluid domain was discretized using the Cartesian cut-cell meshing approach in SolidWorks Flow Simulation, which handles the sharp edges of the skirt windows without producing highly skewed cells [22]. Three meshes were generated: a coarse mesh of 4,177 cells for rapid initial checks, a medium mesh (the project baseline) of 11,840 cells with local refinement around the solid surfaces, and a fine mesh of 127,646 cells to resolve the boundary layers on the stems and the air-bleed regions. From the cell counts N, the effective three-dimensional refinement ratios $r = (N_{fine}/N_{coarse})^{1/3}$ are 1.42 between the coarse and medium meshes and 2.21 between the medium and fine meshes. These are effective values because cut-cell refinement is local rather than uniform.

Numerical Solver Setup, Boundary Conditions, and Engineering Goals:

The flow was modeled as steady, incompressible, and three-dimensional with the Reynolds-averaged Navier–Stokes equations. Turbulence was modeled using the k–ε model with damping functions (Lam–Bremhorst type) and the modified wall functions implemented in SolidWorks Flow Simulation [23][24]. The fluid was air at 101,325 Pa and 293.2 K. With density $\varrho = 1.204$ kg/m^3, dynamic viscosity $\mu = 1.825\times10^{-5}$ Pa·s, freestream velocity U = 20 m/s and maximum skirt diameter D, the Reynolds number is:

$$Re = \varrho\, U\, D / \mu \qquad (4)$$

which gives Re ≈ 8.7×10^4 for D = 66 mm recalculate with the actual D. The dynamic pressure $q = \frac{1}{2}\varrho U^2 = 240.8$ Pa is used to normalize pressure and shear stress in the results. The solver goals were the axial drag force F_d and the lateral lift force F_l. The solution was considered converged when

Table 3. Boundary Conditions and Solver Settings

Boundary	Condition Type	Numerical Value	Vector Direction / Remarks
Domain Inlet	Velocity Inlet	20 m/s	Parallel to longitudinal axis (0° Angle of Attack)
Domain Outlet	Static Pressure	101,325 Pa	Environmental Reference
Shuttlecock Walls	No-Slip Wall	0 m/s	Solid Boundary Constraint
Domain Perimeters	Free-Slip Walls	Frictionless	Eliminates tunnel wall boundary layers
Working fluid	Air, ideal gas	293.2 K, 101,325 Pa	Initial and ambient condition
Flow model	Steady, incompressible, fully turbulent	Re ≈ 8.7×10^4	Based on D and U = 20 m/s

Turbulence model	k–ε with damping functions	Modified wall functions	SolidWorks Flow Simulation [24][23]
Inlet turbulence	intensity, length scale	Solver default, intensity 0.1 %	Value used in the solver
Thermal wall condition	adiabatic or as set	Adiabatic	Heat conduction in solid
Convergence criterion	goal criterion and interval	47 / 66 / 147	Goals: F_d and F_l

The shuttlecock surfaces were assigned a no-slip wall condition, and the structure was assumed to be perfectly rigid. The convergence history of F_d and F_l was monitored as the iterations progressed, and the solver was stopped when the convergence criterion specified in Table 3 was satisfied. The convergence histories, mesh matrix, and final forces for each mesh are presented in the Results and Discussion section.

Results and Discussion:

Grid Convergence and Mesh Independence Verification:

A mesh-sensitivity study was carried out on three meshes: coarse, medium (project baseline) and fine. The monitored quantities were the axial drag force F_d and the lateral lift force F_l. The convergence histories are shown in Figure 3, and the coarse, medium and fine meshes converged within 47, 66 and 147 iterations, respectively (Table 4).

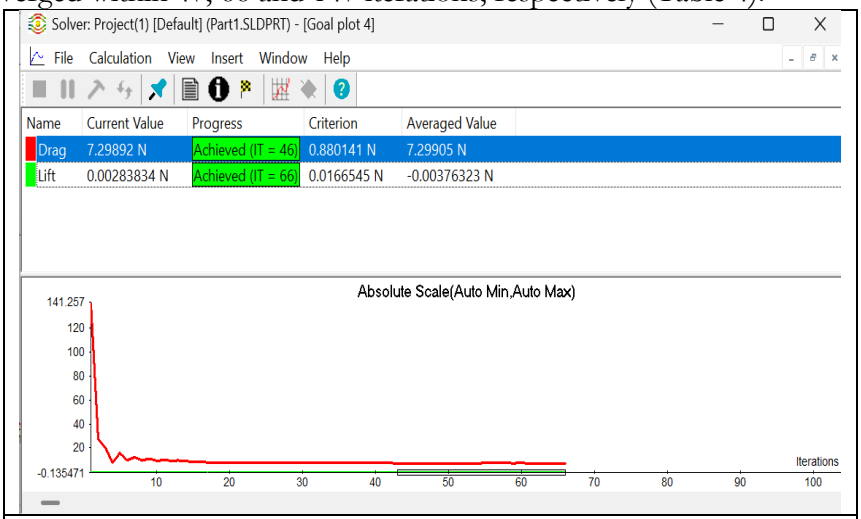

(a)

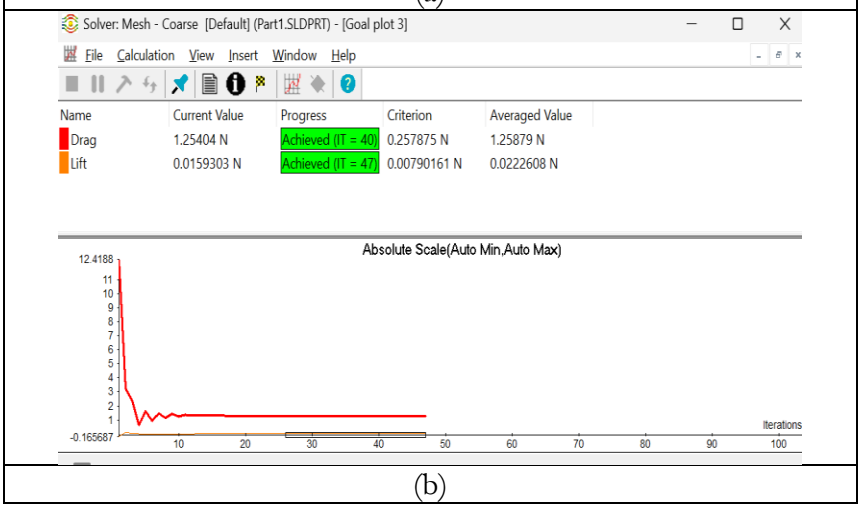

(b)

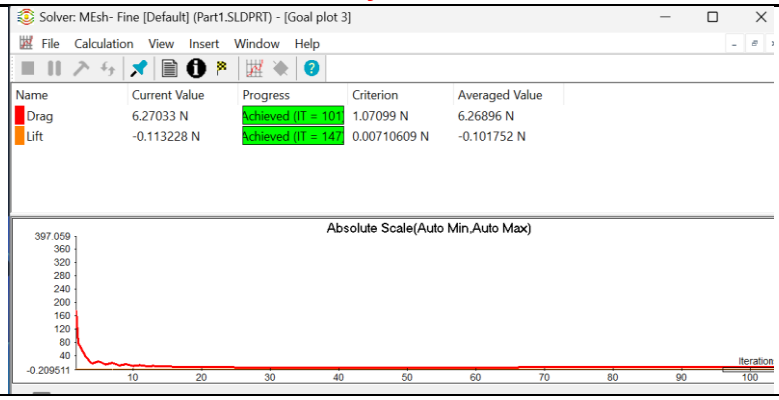

©

Figure 3. Convergence history of the solver goal (force [N] versus iteration number) across mesh configurations: (a) intermediate "Project (1)" mesh, (b) coarse mesh, reaching stable convergence within 47 iterations, and (c) fine mesh, demonstrating narrower residual scatter and stable asymptotic behavior extending to 147 iterations

The forces for each mesh are summarized in Table 4, and the differences between meshes are assessed quantitatively in Table 5.

Table 4. Mesh Independence Matrix and Aerodynamic Force Comparison

Mesh Configuration	Drag Force (Fd) Current [N]	Drag Force (Fd) Averaged [N]	Lift Force (Fl) Current [N]	Lift Force (Fl) Averaged [N]	Convergence Iterations
Mesh - Coarse	1.25404	1.25879	0.01590	0.02226	47
Mesh - (Intermediate)	7.29892	7.29905	0.00284	-0.00376	66
Mesh - Fine	6.27033	6.26896	-0.11323	-0.10175	147

From the coarse to the medium mesh, the averaged drag rose from 1.259 N to 7.299 N, an increase of 479.8% relative to the coarse value, which shows that the coarse mesh does not resolve the separation and air-bleed regions. Refining further to 127,646 cells reduced the drag to 6.269 N, a change of −1.030 N, or 14.1 % of the medium-mesh value (16.4 % of the fine-mesh value). The drag therefore does not approach a limit monotonically: the ratio of successive differences, $R = (F_{d,fine} - F_{d,medium})/(F_{d,medium} - F_{d,coarse}) = -0.17$, is negative, which indicates oscillatory convergence [19]. The Grid Convergence Index and Richardson extrapolation require monotonic convergence on grids in the asymptotic range, so they cannot be applied reliably to these three meshes, and no discretization-error band is claimed. The lift force remained small relative to the drag on all meshes (below 2 % of F_d), which is consistent with a nearly symmetric flow at 0° angle of attack.

The likely contributors to the 14.1% difference are as follows. (i) The thin skirt windows are resolved by only a few cells on the coarse and medium meshes, so the through-flow, and with it the pressure difference across the skirt, changes as the windows become better resolved [5]. (ii) The effective refinement ratio between the medium and fine meshes (2.21) is large and non-uniform, so the three meshes are not a systematically refined family. (iii) A steady RANS solution of a separated wake is sensitive to the size and position of the recirculation zone, which may change with the mesh [4][7]. These explanations are inferences and have not been isolated by additional simulations. The present results show mesh sensitivity and a decreasing trend between the two finest meshes, but they do not show mesh

independence. A further, finer mesh with a uniform refinement ratio above 1.3 [19] is needed before a GCI can be reported.

Table 5. Quantitative Mesh-Sensitivity Assessment of the Averaged Drag Force

Quantity	Coarse → Medium	Medium → Fine
Cell counts	4,177 → 11,840	11,840 → 127,646
Effective refinement ratio, r	1.42	2.21
Change in averaged F_d [N]	+6.040	-1.030
Relative change with respect to the coarser mesh [%]	479.8	14.1
Relative change with respect to the finer mesh [%]	82.8	16.4
Convergence ratio, R	-0.17	-0.17 (R < 0)
Type of convergence	oscillatory	Oscillatory
Grid Convergence Index	Not computed	Not computed (not in the asymptotic range)

Comparison with Published Studies:

To assess the accuracy of the model, the predicted drag was compared with published results (Table 6). The drag coefficient is defined as:

$$C_d = 2F_d / (\rho U^2 A) \quad (5)$$

where A is the reference area, taken here as the frontal area based on the maximum skirt diameter, $A = \pi D^2/4$. For the shuttlecock of [4] (D = 66 mm, $A = 3.42\times10^{-3}$ m²) and the dynamic pressure of 240.8 Pa, the drag forces from the three meshes correspond to $C_d = 1.53$ (coarse), 8.86 (medium) and 7.61 (fine). published drag-coefficient values for feather and synthetic shuttlecocks range from approximately 0.43 to 0.74 [4][1][9], which corresponds to a drag of about 0.4–0.6 N at 20 m/s for this size of shuttlecock.

The predicted drag is therefore about an order of magnitude higher than published data, and the model is not validated in absolute terms. Possible causes, none of which have been isolated, include: a force goal that includes contributions not representative of a free-flying shuttlecock; a model that is larger than the reference shuttlecock (in which case A must be recalculated and the comparison repeated); insufficient mesh resolution of the thin skirt and the stagnation region; and the limits of steady RANS for a separated wake. Two further signs of under-resolution are that the peak pressure coefficient on the nose cap is $C_p = 0.40$ (Eq. (6)), whereas the ideal stagnation value is 1.0, and that the peak velocity of 21.9 m/s is only 1.095 times the freestream velocity. Until these points are resolved, the absolute drag values should be regarded as unvalidated, and only the qualitative flow features are interpreted below.

The pressure coefficient used above is defined as:

$$C_p = (p - p_\infty) / (\tfrac{1}{2} \rho U^2) \quad (6)$$

where p is the local surface pressure [Pa] and $p_\infty = 101{,}325$ Pa is the ambient pressure.

The temperature field passes a simple consistency check. The peak static temperature of 293.39 K is 0.19 K above the assumed ambient temperature of 293.2 K, close to the stagnation temperature rise $U^2/(2c_p) = 0.20$ K, so the energy equation is solved consistently. This check does not validate the drag force. The wake characteristics could not be compared with published data because no wake velocity profiles were extracted from the present simulations.

Table 6. Comparison of the Present Drag Results with Published Data

Source	Method	Speed or Re	Drag coefficient, C_d	Remark
Cooke [1], as summarized in [4]	Wind tunnel, freely rotating feather shuttlecock	3-44 m/s	0.48	Lowest published value
Wind-tunnel studies summarized in [4]	Wind tunnel, feather shuttlecocks	-	0.48-0.74	Wide scatter attributed partly to sting mounts
Solid cone, 20° half angle [4]	Handbook value	-	0.43	Solid (non-porous) reference
[9]	CFD, feather and foam shuttlecocks	Several speeds	0.56	Pitch-angle study
Present study, coarse mesh	Steady RANS, SolidWorks Flow Simulation	20 m/s, Re ≈ 8.7×10^4	1.53 (D = 66 mm)	Not validated
Present study, medium mesh	Steady RANS, SolidWorks Flow Simulation	20 m/s, Re ≈ 8.7×10^4	8.86 (D = 66 mm)	Not validated
Present study, fine mesh	Steady RANS, SolidWorks Flow Simulation	20 m/s, Re ≈ 8.7×10^4	7.61 (D = 66 mm)	Not validated

Aerodynamic Surface Pressure Distribution:

The external field pressure contours mapped across the multi-body synthetic shuttlecock assembly reveal a distinct aerodynamic footprint characterized by distinct pressure differences between the leading nose structure and the trailing skirt. The surface pressure contours are shown in Figure 4.

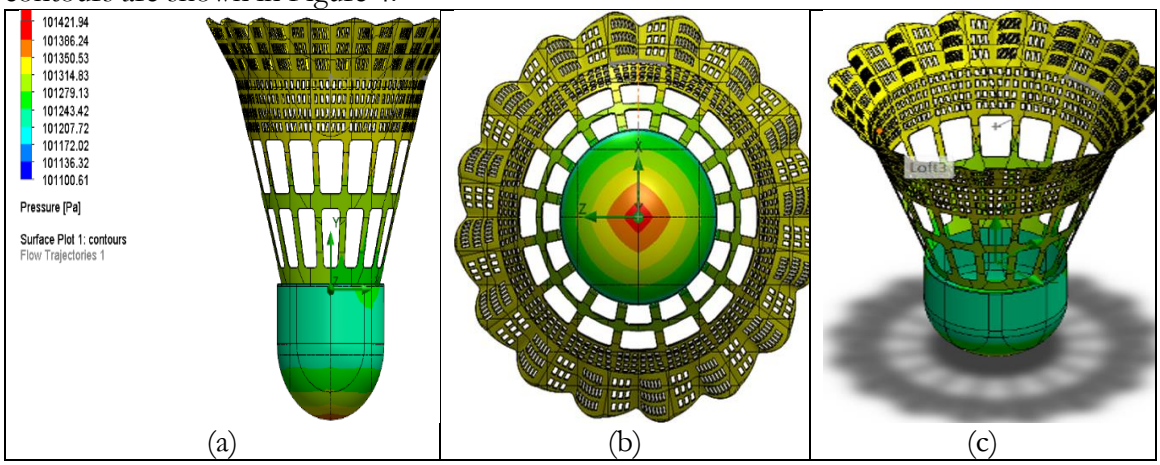

Figure 4. Multi-angle surface pressure contours [Pa] across the synthetic shuttlecock (absolute pressure; legend range 101,100.61 to 101,421.94 Pa):
(a) Longitudinal Side Profile View, **(b)** Frontal Stagnation View, and **(c)** Isometric Cavity View.

Nose Cap Stagnation Zone: As illustrated in the front and profile views, the absolute maximum pressure of 101,421.94 Pa occurs at the apex of the hemispherical nose cap. This high-pressure focus is the primary flow stagnation point, where the incoming air velocity falls to zero and kinetic energy is converted into static pressure. The peak is 96.94 Pa above the ambient pressure of 101,325 Pa, which is a pressure coefficient of C_p = 0.40. The ideal

stagnation value is 1.0 (a rise of 240.8 Pa at 20 m/s), so the computed peak is lower than expected and the stagnation region is probably not fully resolved.

Expansion and Drop off: Moving downstream over the curved profile of the nose cap, the air accelerates rapidly, triggering a sharp pressure drop to approximately 101,243.42 Pa at the transitional junction where the cap meets the forward skirt region (81.58 Pa below ambient, $C_p = -0.34$).

Skirt Permeability and Bleed Profile: Within the interior and exterior surfaces of the trailing skirt lattice, the pressure stabilizes within a narrow band from 101,172.02 Pa down to a localized minimum of 101,100.61 Pa (152.98 to 224.39 Pa below ambient, $C_p = -0.64$ to -0.93). The alternating rectangular and trapezoidal micro-pores bleed air continuously out of the interior cavity, flattening potential low-pressure separation zones. The difference between the nose-cap stagnation pressure and the skirt pressure, about 321 Pa or 1.33 q, is the pressure difference that produces form drag.

Surface Shear Stress and Boundary Layer Interaction:

Surface shear stress contours provide deep insight into localized fluid shear, viscous boundary layer development, and potential flow-separation locations along the solid structural surfaces. The surface shear stress contours are shown in Figure 5.

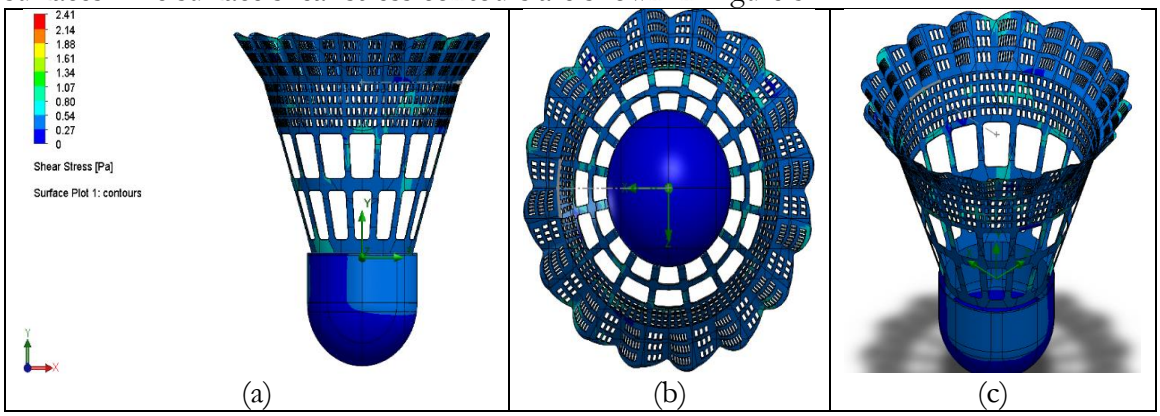

Figure 5. Surface shear stress contours [Pa] displaying viscous friction gradients across the synthetic structure (legend range 0 to 2.41 Pa): (a) Longitudinal Side Profile View, (b) Frontal/Base View, and (c) Isometric Cavity View

Nose Cap Viscous Friction Minimum: The shear stress contours confirm a value of 0 Pa at the front tip of the hemispherical cap. Because the fluid velocity falls to zero at the stagnation point, no wall-normal velocity gradient ($\partial v/\partial y$) exists there and the frictional shear stress vanishes, as expected from theory.

Acceleration Regions and Stem Peaks: The absolute maximum surface shear stress of 2.41 Pa is concentrated along the outer edges of the main longitudinal stems and the primary ring frame. As air is squeezed around the widening cone of the skirt, it accelerates over these solid projections, creating thin, high-gradient boundary layers that raise the local skin friction. In coefficient form, $C_f = \tau/q = 0.010$ at the peak.

Lattice Window Buffeting: The rear sub-lattice structures exhibit intermediate, alternating shear values from 0.54 Pa to 1.34 Pa ($C_f = 0.0022$ to 0.0056). These patterns show the localized shear that occurs where air jets leave the interior cavity through the window slots and meet the external boundary layer. The peak shear stress is about 1 % of the dynamic pressure, whereas the pressure difference across the shuttlecock is about 1.3 q, so form drag dominates over skin friction.

Global Flow Field Visualizations: Cut Plots and Flow Trajectories:

To fully evaluate the fluid-flow interactions with the shuttlecock geometry and the development of the trailing aerodynamic wake, two-dimensional planes (Cut Plots) and three-

dimensional fluid particles (Flow Trajectories) were extracted across the primary longitudinal flow field. The panels are shown in Figure 6.

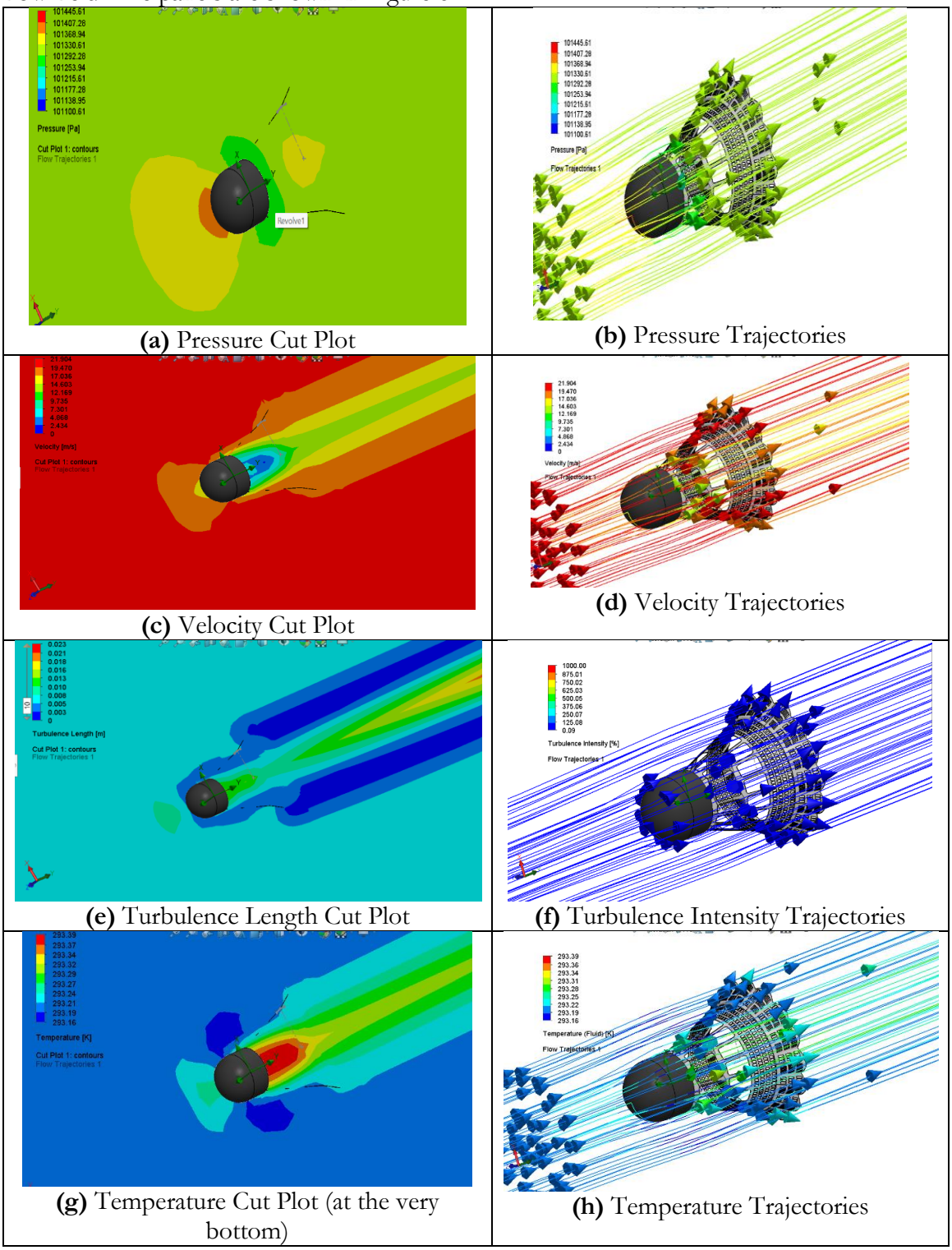

(a) Pressure Cut Plot

(b) Pressure Trajectories

(c) Velocity Cut Plot

(d) Velocity Trajectories

(e) Turbulence Length Cut Plot

(f) Turbulence Intensity Trajectories

(g) Temperature Cut Plot (at the very bottom)

(h) Temperature Trajectories

Figure 6. Flow field characteristics across the assembly: (a) pressure cut plot [Pa], (b) pressure trajectories [Pa], (c) velocity cut plot [m/s], (d) velocity trajectories [m/s], (e) turbulence length cut plot [m], (f) turbulence intensity trajectories [%], (g) temperature cut plot [K], and (h) temperature trajectories [K]. Panels (a), (c), (e) and (g) are cut plots in the longitudinal plane, and panels (b), (d), (f) and (h) are flow trajectories colored by the same quantity.

Pressure Field Interactions:

As visualized in the pressure cut plot and pressure trajectories (Figure 6a,b), a prominent high-pressure field envelops the front of the nose cap, acting as the primary obstruction to the oncoming air. As the flow splits and moves past the hemispherical cap, it expands rapidly over the skirt. The trajectories capture the air-bleed mechanism, showing how a portion of the stream passes directly through the porous lattice openings. This equalizes some of the pressure difference between the inner cavity and the outer boundary layer, which, according to [5], moderates the suction behind the skirt.

Velocity Profiles and Wake Development:

The Velocity Cut Plot and Velocity Trajectories (Figure 6c,d) show the following features of the flow:

Stagnation Point: The velocity drops to 0 m/s at the nose apex (dark blue zone).

Peripheral Acceleration: The fluid accelerates along the outer curvature of the nose cap and the leading edges of the skirt, reaching the domain maximum of 21.904 m/s (red/orange vectors), only 1.095 times the freestream velocity, which is low for flow around a bluff body and is consistent with limited resolution of the cap region.

Recirculation Zone: Immediately behind the solid nose cap and inside the hollow skirt cavity, a large low-velocity zone form (blue core in the cut plot). This low-velocity wake extends downstream of the skirt and is associated with the low-pressure suction region responsible for the drag force (6.27 N on the fine mesh).

Thermal Characteristics and Energy Coupling:

The Temperature Cut Plot and Temperature Trajectories (Figure 6g, h) correlate with the local velocity field, as expected from conservation of total energy in subsonic external flow. As the fluid accelerates over the curvature of the outer geometry, it reaches its minimum static temperature in zones of maximum local velocity. Conversely, the peak static temperature of 293.39 K is found within the low-velocity recirculation wake directly behind the nose cap, where kinetic energy is converted back into thermal energy. This peak is 0.19 K above the assumed ambient temperature of 293.2 K, in line with the stagnation temperature rise of 0.20 K. The temperature gradients are therefore driven by pressure–velocity coupling and not by frictional boundary-layer shearing.

Turbulence and Dissipation Matrix:

The Turbulence Length Cut Plot and Turbulence Intensity Trajectories (Figure 6e,f) show the transition from smooth freestream flow to a turbulent wake. The turbulence length cut plot shows the growth of the shear layers shed from the skirt tip. The turbulence intensity trajectories reach the plot limit of 1000 % inside the trailing wake. Because turbulence intensity is normalized by the local velocity, it becomes very large in near-stagnant regions, so this value indicates a strongly turbulent, low-velocity wake and is not a quantitative measure of turbulence. These steady results do not by themselves demonstrate flight stability, which would require moment coefficients at non-zero angles of attack.

Quantitative Comparison and Aerodynamic Significance:

Table 7 summarizes the main quantities of the fine-mesh solution in dimensional and non-dimensional form, together with their aerodynamic meaning. Pressures are normalized as C_p (Eq. (6)) and shear stress as $C_f = \tau/q$, with $q = 240.8$ Pa.

Table 7. Quantitative Summary of the Fine-Mesh Results and Their Aerodynamic Significance

Quantity	Value	Non-dimensional value	Aerodynamic significance
Peak surface pressure (nose apex)	101,421.94 Pa (+96.94 Pa)	$C_p = 0.40$	Stagnation zone; ideal value is 1.0, so the peak is probably under-resolved
Pressure at cap–skirt junction	101,243.42 Pa (−81.58 Pa)	$C_p = -0.34$	Flow expansion around the cap
Skirt pressure band	101,172.02 to 101,100.61 Pa (−152.98 to −224.39 Pa)	$C_p = -0.64$ to -0.93	Low-pressure skirt and wake region; the front-to-wake difference drives form drag
Peak wall shear stress	2.41 Pa	$C_f = 0.010$	Stems and ring frame; skin friction is small compared with pressure force
Shear stress in lattice region	0.54 to 1.34 Pa	$C_f = 0.0022$ to 0.0056	Jets from the windows meeting the outer boundary layer
Maximum velocity	21.904 m/s	$U/U_\infty = 1.095$	Acceleration over the cap; low value suggests limited resolution
Peak static temperature	293.39 K (+0.19 K)	$\Delta T/\Delta T_0 \approx 0.95$	Consistent with the stagnation temperature rise $U^2/(2c_p) = 0.20$ K
Peak turbulence intensity	1000 % (plot limit)	-	Very low local velocity in the wake; qualitative only
Drag force (fine mesh)	6.269 N	$C_d = 7.61$ (D = 66 mm)	Not validated; about ten times published values
Lift force (fine mesh)	−0.102 N	$\lvert F_l \rvert / F_d = 0.016$	Small compared with drag at 0° angle of attack

Practical Implications:

Design of air bleed: The results indicate that the pressure difference between the nose stagnation region and the skirt wake contributes to pressure drag, and that bleed through the skirt windows moderates the suction behind the skirt. Window size, number, and open-area ratio are therefore likely control parameters for the drag of a synthetic shuttlecock, as found for gap size in [5][10]. A parametric study on a validated model is needed before quantitative design rules can be given.

Aerodynamic stability: The flow trajectories describe the through-flow pattern at 0° angle of attack only. The restoring moment that turns a shuttlecock nose-first, and hence its stability, requires simulations at non-zero angles of attack and the pitching-moment coefficient, which were not computed here.

Future CFD investigations: The mesh-sensitivity results show that a thin-walled perforated skirt needs a finer, uniformly refined mesh than the meshes used here, and that the force goal, reference area and model scale must be checked against published coefficients before the model is used for design comparison.

Recommendations and Future Work:

Verify the force-goal definition, the reference area and the model scale, and recompute the drag coefficient with Eq. (5).

Refine the mesh systematically with a uniform refinement ratio above 1.3 [19], add at least one finer mesh, and report the Grid Convergence Index once monotonic convergence is obtained.

Validate against wind-tunnel drag measurements of the same shuttlecock at the same speeds, using a mount that disturbs the base flow as little as possible [4][10].

Repeat the simulation with a transient or scale-resolving approach [7] and at non-zero angles of attack to obtain unsteady wake data and the pitching moment.

Include skirt flexibility through fluid–structure interaction [8] and carry out a parametric study of window size and open-area ratio once the model is validated.

Conclusion:

A steady-state CFD simulation of an explicitly modeled porous synthetic shuttlecock was carried out at 20 m/s to examine the pressure, shear stress, velocity, turbulence and temperature fields and to test the sensitivity to mesh resolution. The findings below distinguish what the simulations demonstrate from what remains assumed or unverified.

Demonstrated by the Simulations:

Mesh sensitivity: The averaged drag was 1.259 N, 7.299 N and 6.269 N on meshes of 4,177, 11,840 and 127,646 cells. The drag response is oscillatory (R = -0.17) and the medium-to-fine difference is 14.1 %, so mesh independence was not achieved and no GCI is reported.

Pressure Field: The peak surface pressure was 101,421.94 Pa (96.94 Pa above ambient, C_p = 0.40) at the nose apex, and the skirt region lay between 101,172.02 Pa and 101,100.61 Pa (C_p = -0.64 to -0.93). The front-to-wake pressure difference, about 1.3 q, indicates that pressure (form) drag dominates.

Boundary-Layer Dynamics: The peak wall shear stress was 2.41 Pa (C_f = 0.010) on the main stems and ring frame, and the wall shear stress was zero at the nose stagnation point, as expected from fundamental fluid mechanics.

Thermal Behavior: The peak static temperature of 293.39 K lies 0.19 K above ambient, consistent with the stagnation temperature rise of 0.20 K, so the temperature field reflects pressure–velocity coupling and not significant frictional heating.

Flow Structure: A low-velocity recirculation zone forms behind the nose cap and inside the skirt, and the trajectories show air bleeding through the skirt windows at 0° angle of attack.

Not Demonstrated, or Based on Assumptions:

Absolute drag: The drag coefficient implied by the fine-mesh drag (C_d = 7.61 for D = 66 mm) is about ten times the published range of 0.43–0.74, so the absolute force is not validated.

Flight Stability: Passive stability through air bleed was not demonstrated, because no moment coefficient or non-zero angle of attack was simulated.

Turbulence Values: The 1000 % turbulence intensity is a plot limit in a near-stagnant wake, and turbulence quantities are qualitative.

Limitations: The simulations are steady RANS, so wake unsteadiness is not resolved; a single speed (20 m/s) and angle of attack (0°) were considered; the skirt was assumed rigid; the mesh resolution of the thin skirt and the stagnation region is limited; and no experimental validation was performed. These limitations, and the recommendations above, define the next steps for this work.

Funding:

This research received no funding.

References:

[1] Alison J. Cooke, "Shuttlecock aerodynamics," *Engineering*, 19999, [Online]. Available: https://www.semanticscholar.org/paper/Shuttlecock-aerodynamics-Cooke/7a056bb4b96f52cacbb411beddc2aaeaf5b85932?p2df

[2] F. Alam, H. Chowdhury, C. Theppadungporn, and A. Subic, "Measurements of aerodynamic properties of badminton shuttlecocks," *Procedia Eng.*, vol. 2, no. 2, pp.

2487–2492, Jun. 2010, doi: 10.1016/J.PROENG.2010.04.020.

[3] H. Hasegawa, S. Kitta, M. Murakami, and S. Obayashi, "Flow analysis and aerodynamic characteristics of a badminton shuttlecock with spin at high Reynolds numbers," *Sport. Eng.*, vol. 16, no. 2, pp. 91–98, Jun. 2013, doi: 10.1007/S12283-013-0112-4.

[4] J. H. Hart, J. R. Potts, and D. J. James, "Comparison of turbulence modelling approaches in simulation of a feather shuttle: a porous conical bluff body," *Sport. Eng. 2018 214*, vol. 21, no. 4, pp. 465–478, Nov. 2018, doi: 10.1007/S12283-018-0293-Y.

[5] C. S. H. Lin, C. K. Chua, and J. H. Yeo, "Aerodynamics of badminton shuttlecock: Characterization of flow around a conical skirt with gaps, behind a hemispherical dome," *J. Wind Eng. Ind. Aerodyn.*, vol. 127, pp. 29–39, Apr. 2014, doi: 10.1016/J.JWEIA.2014.02.002.

[6] A. Verma, A. Desai, and S. Mittal, "Aerodynamics of badminton shuttlecocks," *J. Fluids Struct.*, vol. 41, pp. 89–98, Aug. 2013, doi: 10.1016/J.JFLUIDSTRUCTS.2013.01.009.

[7] J. Hart and J. Potts, "Numerical Investigation of the Flow around a Feather Shuttlecock with Rotation," *Proc. 2020, Vol. 49, Page 28*, vol. 49, no. 1, p. 28, Jun. 2020, doi: 10.3390/PROCEEDINGS2020049028.

[8] D. Zala, H. Dechiraju, and S. Mittal, "Computational analysis of the fluid-structure interactions of a synthetic badminton shuttlecock," *Phys. Fluids*, vol. 36, no. 1, Jan. 2024, doi: 10.1063/5.0182411/2932813.

[9] D. A. Rasid, M. F. Remeli, B. Singh, and H. Moria, "Aerodynamic properties comparison between natural feather, nylon, and synthetic shuttlecocks," *Int. J. Eng. Syst. Model. Simul.*, vol. 16, no. 1, pp. 44–51, 2025, doi: 10.1504/IJESMS.2025.142974.

[10] L. Zhou, "Aerodynamic characteristics and trajectory analysis of badminton shuttlecocks," *Acta Bioeng. Biomech.*, vol. 26, no. 4, pp. 29–37, Dec. 2025, doi: 10.37190/ABB-02508-2024-01.

[11] Y. IMAMATSU, K. NAKAGAWA, H. HASEGAWA, and M. MURAKAMI, "Turnover Stability of a Badminton Shuttlecock during Flip Movement," *Proc. Symp. Sport. Hum. Dyn.*, vol. 2018, no. 0, pp. C–11, 2018, doi: 10.1299/JSMESHD.2018.C-11.

[12] M. Arora and R. Jain, "CFD and Data Analysis of the Shuttlecock: To Evaluate the Correlation Between the Drag Force and Trajectory Parameters," *Lect. Notes Networks Syst.*, vol. 1263 LNNS, pp. 495–506, 2025, doi: 10.1007/978-981-96-2724-0_36/SAVE-RESEARCH.

[13] Z. Zhang, Z. Peng, X. Li, Z. Ma, P. Zhou, and X. Huang, "Shuttlecock trajectory during spin serves," *Phys. Fluids*, vol. 37, no. 8, Aug. 2025, doi: 10.1063/5.0275494/3359548.

[14] M. K. Kansara and S. Mittal, "Wind-tunnel study of the effect of autorotation on feather and nylon badminton shuttlecock," *Phys. Fluids*, vol. 38, no. 9, Sep. 2026, doi: 10.1063/5.0338356/3403634.

[15] H. Ozaki *et al.*, "Comparison of traditional badminton waterfowl-feather shuttlecocks versus synthetic-feather shuttlecocks using different test modalities," *Sport. Eng. 2026 291*, vol. 29, no. 1, pp. 18-, May 2026, doi: 10.1007/S12283-026-00551-W.

[16] T. Woo, F. Alam, and A. Kootsookos, "The scientific development of badminton shuttlecocks: Review paper," *Sustain. Sport. Sci. J.*, vol. 2, no. 3, pp. 149–165, Jun. 2024, doi: 10.55860/ZQQE3823.

[17] S. H. Park, D. H. Seo, and J. H. Jeong, "Experimental and numerical analysis of thermal flow in open-cell porous metal during Darcy-Forchheimer transition regime," *Appl. Therm. Eng.*, vol. 181, p. 116029, Nov. 2020, doi:

10.1016/J.APPLTHERMALENG.2020.116029.
[18] P. J. Boache, "Perspective: A Method for Uniform Reporting of Grid Refinement Studies," *J. Fluids Eng.*, vol. 116, no. 3, pp. 405–413, Sep. 1994, doi: 10.1115/1.2910291.
[19] I. B. Celik, U. Ghia, P. J. Roache, C. J. Freitas, H. Coleman, and P. E. Raad, "Procedure for estimation and reporting of uncertainty due to discretization in CFD applications," *J. Fluids Eng. Trans. ASME*, vol. 130, no. 7, pp. 0780011–0780014, Jul. 2008, doi: 10.1115/1.2960953/444689.
[20] G. Vivarelli, N. Qin, and S. Shahpar, "A Review of Mesh Adaptation Technology Applied to Computational Fluid Dynamics," *Fluids*, vol. 10, no. 5, May 2025, doi: 10.3390/FLUIDS10050129.
[21] X. Zhang, M. Savoie, M. K. Quinn, B. Parslew, and A. Revell, "Simulation of Flow Around a Finite Rectangular Prism: Influence of Mesh, Model, and Subgrid Length Scale," *Entropy 2025, Vol. 27, Page 65*, vol. 27, no. 1, p. 65, Jan. 2025, doi: 10.3390/E27010065.
[22] H. J. Lee and J. J. Kim, "Enhancing geometric fidelity and wind-field prediction accuracy in complex urban environments using a Cartesian cut-cell CFD model," *Sustain. Cities Soc.*, vol. 140, p. 107247, Apr. 2026, doi: 10.1016/J.SCS.2026.107247.
[23] "SOLIDWORKS Flow Simulation".
[24] Lam, C. K. G., and Bremhorst, K., "A Modified Form of the k-ε Model for Predicting Wall Turbulence," *ASME. J. Fluids Eng*, vol. 10, no. 3, pp. 456–460, 1981, doi: https://doi.org/10.1115/1.3240815.

Copyright © by authors and 50Sea. This work is licensed under Creative Commons Attribution 4.0 International License.